Open Journal of Fluid Dynamics, 2022, 12, 127-153
https://www.scirp.org/journal/ojfd
ISSN Online: 2165-3860
ISSN Print: 2165-3852

Vortex Shedding Lock-in on Tapered Poles with Polygonal Cross-Section

Jaime A. Ocampo[1*], Steven H. Collicott[1], Robert J. Connor[2]

[1]School of Aeronautics and Astronautics, Purdue University, West Lafayette, USA
[2]Lyles School of Civil Engineering, Purdue University, West Lafayette, USA
Email: *collicott@purdue.edu

How to cite this paper: Ocampo, J.A., Collicott, S.H. and Connor, R.J. (2022) Vortex Shedding Lock-in on Tapered Poles with Polygonal Cross-Section. *Open Journal of Fluid Dynamics*, **12**, 127-153.
https://doi.org/10.4236/ojfd.2022.122007

Received: October 9, 2021
Accepted: April 26, 2022
Published: April 29, 2022

Abstract

A study to investigate the effects of taper on vortex shedding coherence on High Mast Lighting Towers (HMLT) with models of eight-, twelve-, and sixteen-sided polygonal cross-section was performed in Purdue's Boeing Low-Speed Wind Tunnel. Partial tower models were mounted on springs to recreate a flutter phenomenon seen on high mast lighting towers and data was taken using a stationary configuration within the wind tunnel. The model was later oscillated at specified frequencies and amplitudes and the resulting wake and surface pressures were recorded and compared to the stationary cases. The researchers aim to study the characteristics of a "lock-in" phenomenon, that is, a region of pole height where there is a vortex cell with a single shedding frequency, instead of different shedding frequencies for different diameters as Strouhal theory dictates. Results show the existence of vortex cell shedding for clamped models. Using a motor and a forcing cam to recreate the elastic movement of the HMLT in ambient conditions has yielded a specific range of diameters to determine the size of the locked in vortex cells. According to standard Department of Transportation manufacturing standards for tapered HMLT, the lock in distance for small excitations (0.254 cm) would be approximately 305 cm in tower height.

Keywords

Vortex Shedding, Lock-In, Tower Aerodynamics

1. Introduction

The effect of crosswind oscillations on high mast lighting towers (HMLT) is an important phenomenon for study by civil and highway engineers. The results of these aerodynamic studies can help engineers develop tools to design these structures so they can withstand the high life-cycle stresses caused by crosswind oscillations.

HMLT is typically installed adjacent to interstate interchanges and exits ramps. The towers are produced by numerous fabricators and are between 30 and 45 m tall, have a diameter at the base of approximately 60 to 75 cm, and have a tip diameter between approximately 20 and 30 cm. The poles are primarily made with a dodecagonal or hexadecagonal steel cross-section. Some previous work was found with tapered 8-sided poles so the three cross-sections tested for this research are 8-, 12-, and 16-sided. For brevity in this paper, only the 12-sided results are shown. One example of a 12-sided tower is shown in Figure 1. Several failures have been reported in the literature that have been attributed to fatigue cracking as a result of vortex shedding and other wind loadings.

Figure 1. Typical high mast lighting tower (HMLT).

The work presented in this document seeks to describe the aerodynamic flow structure of these HMLT by reproducing some of the HMLT behavior in a lab environment with a wind tunnel. The initial stage of this project was analyzing the behavior of these HMLT with respect to high crosswind conditions. This project was conducted in a joint effort with civil engineers at Purdue. The civil engineers conducted field tests on some of these HMLT throughout the country and gathered data when the tower reached a certain level of excitation. Direct one-to-one comparisons between field and wind tunnel were not attempted because the necessary scaling of both aerodynamic and mechanical parameters proved impractical.

This aerodynamic study includes pressures and wakes data during pole excitation caused by vortex shedding cells. These cells consist of a range of diameters of the tapered structure having the same shedding frequency and thus not being described by the Strouhal equation. A representation clarified with lines for each vortex pair can be seen in **Figure 2**. In the case of the Strouhal relation [1] [2], every diameter should have its own specific frequency and the tower would have a range of frequencies for a single velocity. When one of these shedding frequencies

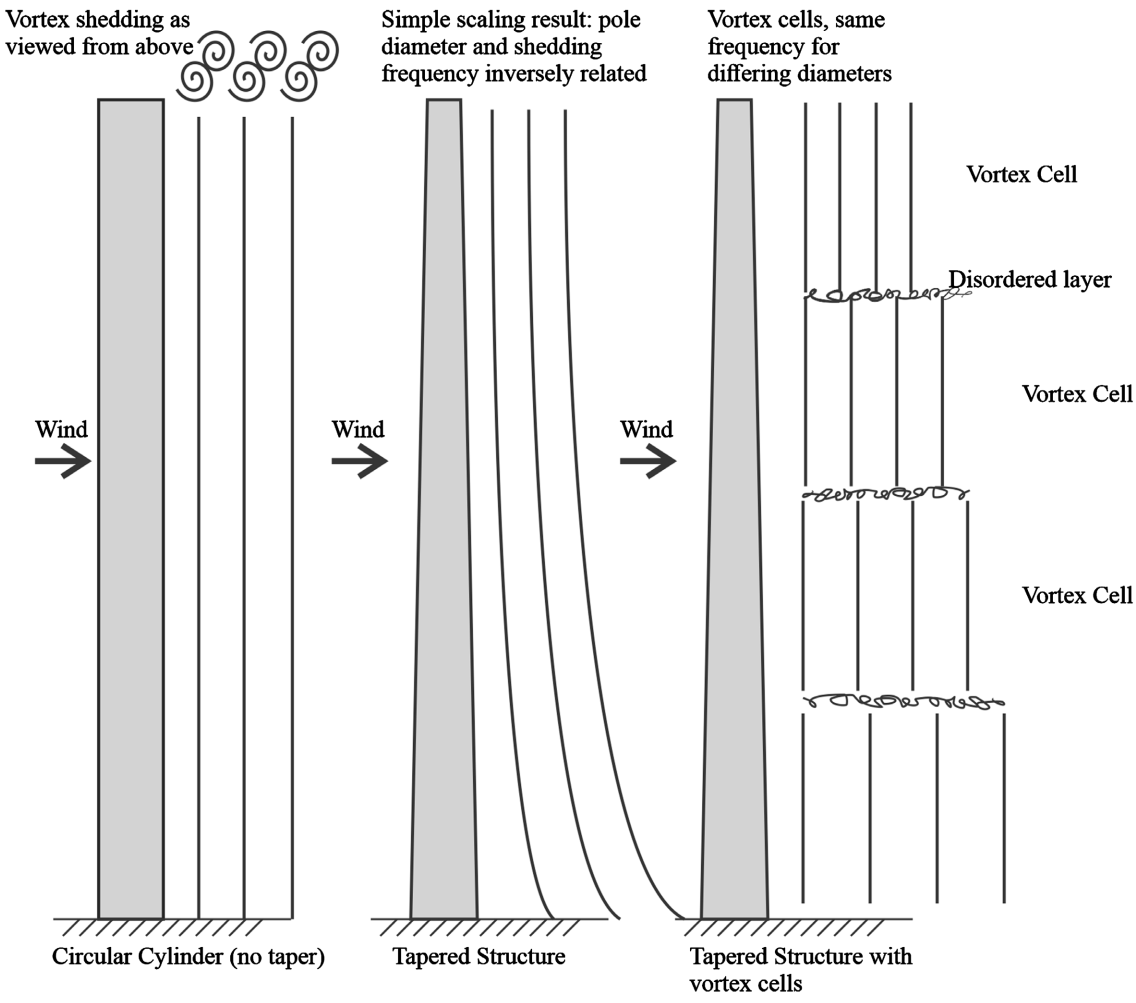

Figure 2. Vortex shedding on three different poles.

is near a natural frequency of the structure, the results can be dangerous. The structure starts to use the wind energy and converts it into strain and kinetic energy with growing amplitude; over time, this high amplitude results in fatigue cracking at welded details particularly at the base of the pole. If permitted to grow unchecked, these cracks have resulted in collapse of several poles across the USA [3] [4] [5].

2. Previous Literature

2.1. Polygonal Cross-Section Studies

There are few papers that address experimental analysis of effects of the cross-sections relevant to this study [6] [7]. A 1985 review paper [6] discusses the dissimilarity between square and circular cross-sections as two differences. There is a broad peak in the plot of amplitude versus velocity plot for the square cross section while the circular cross section has a narrow peak. This happens because the square cross section has a spilled vortex on the back of the structure. Flow separation on both structures is dissimilar for the different cross sections.

These observations may imply that the peak shape in the spectrum narrows as the shape starts to resemble a circle. Another research effort and one of the most important on this section is the Iowa Report [8] for the Department of Transportation. This paper includes several of the same prerequisites of the current research and does a great job analyzing 2-D shedding on a dodecagonal cylinder; however, they neglect 3-D effects such as vortex cells and taper. The study is done with a static and dynamic mode (force balance and free vibration) and the study is centered on the responses in amplitude and Strouhal number. An important conclusion drawn from this study was that the structure was primarily affected in the second mode, contrary to the AASHTO code which only considers the fundamental frequency of the structure.

There are four different domains for this type of vortex shedding: subcritical, critical, transcritical, and supercritical [9]. At the sub and super-critical regime, there is an established vortex shedding pattern with a unique frequency as known in a classical Karman vortex street. The critical location defines the boundary between the subcritical and transcritical regions, and the transcritical range defines an area where the flow is disorganized and does not give a steady shedding frequency.

A study at Iowa State University [10] used experimental data for hexadecagonal cylinders found in the literature review. The study is done at 105 < Re < 106 and the data includes Strouhal number charts for several hexadecagonal cylinders with different corner radii. The corner radius seems to influence measurements when the Reynolds number is above that required for subcritical vortex shedding and below the minimum Reynolds number for supercritical shedding. That is, the corner radius defines the critical and trans-critical regime. Of interest, the differences between cylindrical and hexadecagonal cross-section affect the Reynolds number boundaries where shedding exists by factors of 2 to 4 depending on the corner radius, however, as the radius is increased to 75% of the radius of the inscribed circle, the differences are almost null between the hexadecagonal and circular cylinder. Also, the difference in Strouhal number within the shedding ranges is very small. This study however, does not include within its scope 3-D effects or taper, but is a great comparison for cross-sectional shapes.

Other studies have been done on non-circular cylinders, such as a comprehensive experimental paper on different polygonal shapes [11] (103 < Re < 104), where fifty-three models where built and tested on a force balance. The polygonal shapes tested include circular, hexagonal, and octagonal and show an interesting trend in Strouhal number with taper. In the circular cross section case, the Strouhal number changes dramatically for different tapers, however, for the octagonal case; the Strouhal number only changes ≈ ±0.01.

2.2. Taper Studies

The taper effects section focuses on what other people have done to take into account taper in their computations, e.g., [12] [13] [14] [15]. In [12] the author, with no specific Reynolds number range, dissects the structure into nodes and calculates the shedding frequency for each of these nodes and uses a 10% Reynolds number range to determine which nodes are affected by lock-in and which ones are not. He then proceeds to calculate the forces on these nodes. However, this method neglects any kind of 3-D effects. This method may be inaccurate considering it uses an average Strouhal number for circular cross sections used is 0.18 while most other papers use 0.2 - 0.22.

Vickery and Clark [13] (Re ~ 104) also contribute knowledge to the taper problem by including a pressure tap study. Their conclusions state that "the excitation of the second mode may be critical for the upper part of the [chimney] stack". It is also acknowledged that there is a span-wise variation in frequency. Their data shows several regions where shedding frequency has the same value for different diameters. These regions are indicative of lock-in and are present in both turbulent and smooth flows; unfortunately, these results are not explained but discarded as "irregularities" (**Figure 3**). The fluctuating surface pressure studies also include turbulence levels with height and their study also concludes that there may be more excitation on the second mode than the fundamental mode.

3. Experimental Setup

This section describes the hardware, software, and instrumentation that were used to gather the data.

3.1. Hardware

The hardware includes the models, the oscillation rig, the model mount, and the driving motor. The overall apparatus setup is shown in **Figure 4**. Some pictures

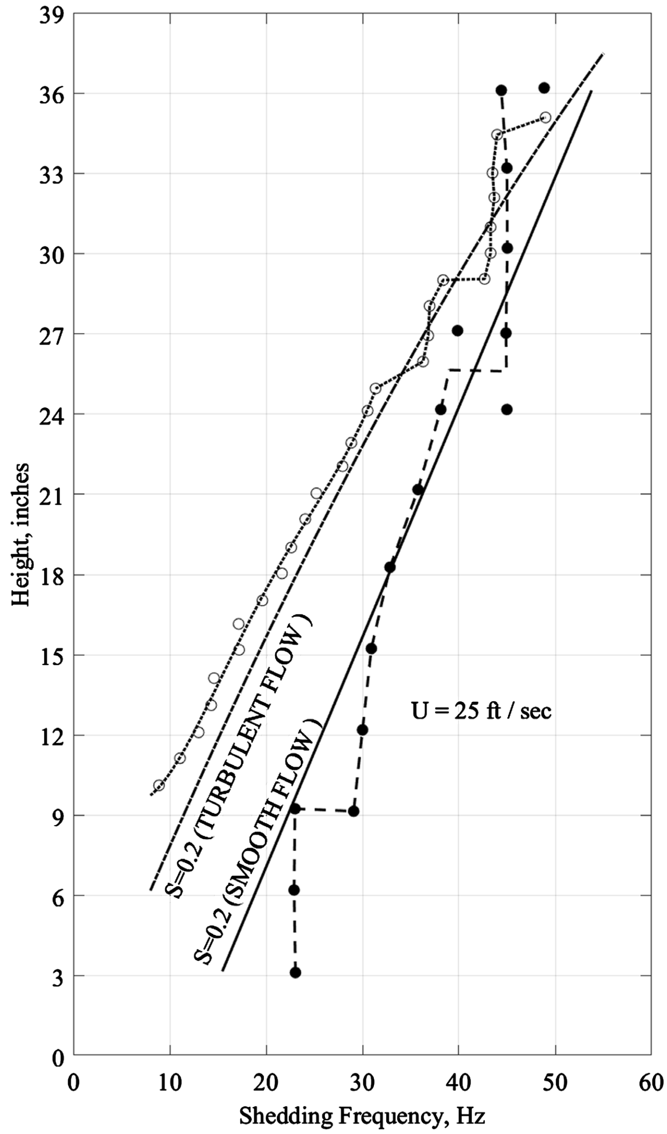

Figure 3. Lock-in shown by [13] (reproduced in modern format). The smooth and turbulent lines show the frequencies when calculated by the Strouhal relation in 2-D while the points show several areas with the same shedding frequency and different diameters.

of the setup are also shown in **Figure 5** and **Figure 6**.

3.1.1. Overall Setup

In **Figure 5**, the overall set up is shown. The oscillation rig (underneath the tunnel) is made up of an iron and aluminum structure to hold everything in place and is attached directly to the wind tunnel. The oscillation piece is comprised of two 0.5-inch bars that hold the model mount (the airfoil extrusions that enter into the tunnel) and uses four springs around two 0.5-inch bars on each side that define the system natural frequency. There is a square bar connected to the 0.5-inch bars through linear rollers to reduce friction, there is one roller per 0.5-inch bar and four #6 - 32 bolts that connect each linear roller to the square bar.

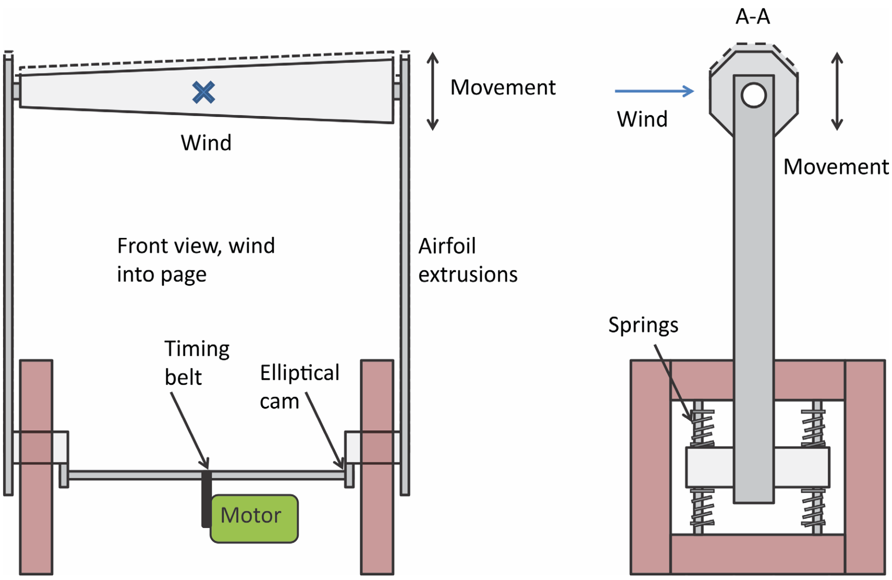

Figure 4. Schematic of overall set up.

Figure 5. Overall set up fo rthe model and hardware.

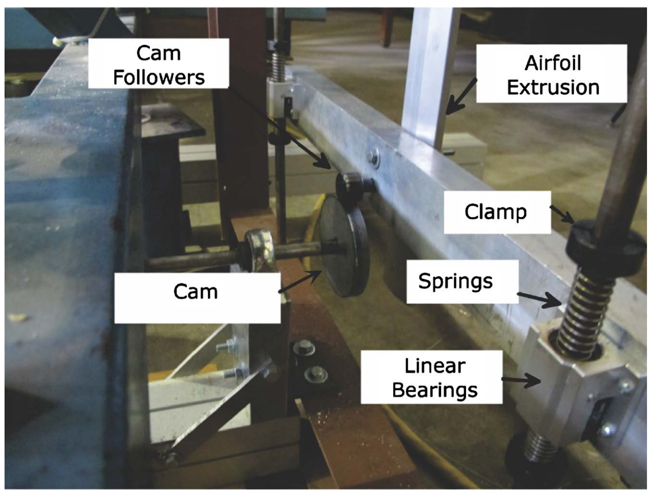

Figure 6. Close up view of the spring and the oscillatin hardware.

3.1.2. Models

There are three models: 8-, 12-, and 16-sided cross-section models. The three models are 152.4 cm long, have a taper ratio of 0.00117 cm/cm and a diameter at the span-wise center of 12.7 cm. These have all been tested inside the tunnel using both the hot wires and low sampling speed pressure scanner.

The three models are made with fiberglass skinned foam core panels for the outer section and these pieces are supported by wood ribs, the connection between the foam core panel and wood ribs is done using a set of interlocking wood pieces. The whole assembly rests on a 3.18 cm diameter aluminum tube. The aluminum tube includes openings for the vinyl tubing that leads to the pressure scanner.

The models are equipped with pressure taps, a total of 31 pressure taps for the 8 sided model and 23 taps for the 12 and 16 sided. The configuration for these taps are, for the 8-sided model: 7 rows near the span-wise center separated by 2.54 cm span-wise with two extra pressure taps on either side of each row and 5 taps in the span-wise direction at locations ±20.3, 25.4, 30.5, 35.6, 40.6 cm from the span-wise center. The 12- and 16-sided models each have 13 taps near the center separated by 1.27 cm inch in the span-wise direction and pressure taps at locations ±20.3, 25.4, 30.5, 35.6, 40.6 cm from the span-wise center, as shown in **Figure 7**.

3.1.3. Forcing Mechanism

The forcing mechanism consists of a steel shaft, four rotation bearings, a 12VDC motor, two timing pulleys, a timing belt, and two aluminum cams. The aluminum cams transfer rotational energy to linear kinetic energy, here, delta denotes the difference between the largest and smallest radii on the cam. The cams are designed with an elliptical shape so one revolution has a total of two complete oscillation waves. Initially, the cams were designed to create a 2.54 cm range of amplitude, later, two other cams, one with 1.27 cm range and another with 0.254 cm delta were included.

The motor is connected to the steel shaft using two timing belt pulleys set in a 3:1 ratio, thus decreasing the maximum rotational speed of the shaft from 1800 RPM to 600 RPM (10 revolutions per second at 2 waves per revolution, gives maximum 20 Hz motion).

3.2. Instrumentation and Sensors

For the present study three different sets of instruments are being used. The sensors are a 16-channel pressure scanner and two hot wire anemometers. The

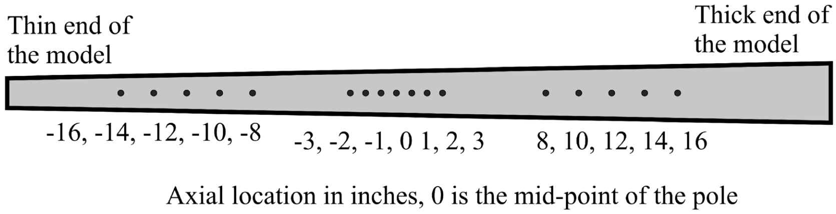

Figure 7. Spanwise pressure tap locations for all models.

first type of sensor was a PSI-ESP with 16 channels and maximum pressure of 4 inches of water. The first hot wire probe was connected to a Bruhn CTA box which regulated the resistance and voltage as well as provided a power source. The output from the Bruhn was then stored using a LeCroy WaveJet 314A. The second hot wire probe was connected to an Intelligent Flow Analyzer (IFA-100). The waveforms were then post-processed. The hot wire instrumentation was used in different configurations depending on what data was relevant to the flow under study, and the configuration used for the data in this paper is shown in **Figure 8**. In this image, both hot wire probe supports are mounted on a movable traverse. The traverse is motorized, with a P315X stepper/indexer and motor system. The whole assembly can be moved in the x (spanwise) and y (crosswind) directions (with the downstream direction as z).

Another study was done using a water tunnel and dye. The dye was used to show the macroscopic structure of the flow. The vortex shedding frequency of the model is around 16 Hz which is too fast to capture using a standard camera, however, in water, the Reynolds number requires a much lower velocity. The dye can be used to examine the height-wise (spanwise) movement of the flow (or an "updraft" on a tower). The dye can be also used to identify the span-wise locations that contain the interface between vortex shedding cells.

4. Results and Discussion

For the cases in this paper, only the 0.254 cm amplitude cams and the stationary cases are shown, with other results archived [5] [16]. The results in this section show some of the more interesting behavior seen in the flow over the 12-sided models. In these cases, the independent variable is the height-wise location on the tower where negative numbers are the thin end of the model, and positive, the thick end of the model.

4.1. Aeroelastic Lock-in vs. Aerodynamic Vortex Cells

Figure 9 shows the characteristic frequencies of the 12-sided model in the vertex upwind configuration being excited at a frequency below the shedding frequency for the stationary case (the stationary case is a clamped case where no forcing is being applied from the oscillation rig at the same aerodynamic conditions). In

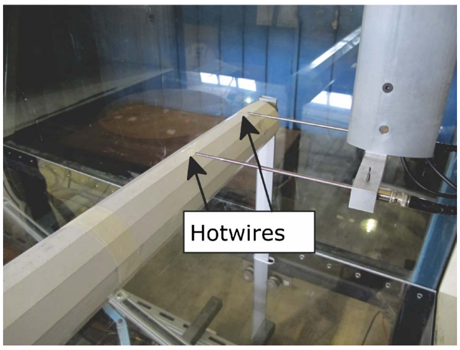

Figure 8. Hot-wires as mounted on the traverse. Flow is from left to right in this view.

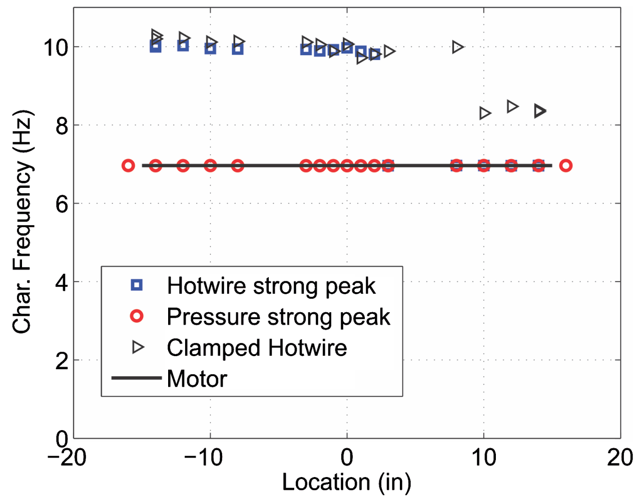

Figure 9. Results showing lock-in on 12-sided model in vertex-upwind orientation, Re = 44,000 ± 2000.

this figure, the stationary case and forcing cases have approximately the same frequencies on the thin end of the model. This means the aerodynamic shedding frequency is setting the frequency of the vortex cell and not the forcing frequency of the oscillation rig. The primary frequency for the pressure (which originates on the actual structure and would be most affected by the forcing excitation) is exactly that of the forcing oscillation. For the measurements near the middle of the model, there are some frequency changes between the stationary and forcing frequencies. Then, finally, the hot wire frequency becomes that of the forcing excitation at the thicker end of the model.

There are two large differences between the forcing case and the stationary case. The first difference is the location where the frequency switches (also known as the vortex cell boundary). In the forcing case, it seems to be at the middle of the model and on the stationary case it is between 3 and 8 inches. This shows further proof that the aeroelastic movement of the structure does have the ability to change the aerodynamic structure of the wake of the body. These results are repeatable. The second difference is the actual frequency of the second vortex cell: in the stationary case, the thicker end vortex cell is at approximately 8 - 8.5 Hz, while in the forcing case the frequency has shifted to a frequency of 7 Hz. This means that the forcing case may be increasing the size of the stationary case vortex cell seen on the thick end but increasing the size of another vortex cell further on the thick end of the model (a higher diameter means lower frequency).

Figure 10 shows the signal strength. The black line in Figure 10 represents the forcing frequency. In this case some of the primary pressure and forcing case pressure readings are so high (almost an order of magnitude higher than those shown here) that they were cropped to allow for reasonable axes. It seems that the primary signal strength of the hot wire for the stationary model case is comparable to that of the hot wire forced case meaning that the results at the 10 Hz

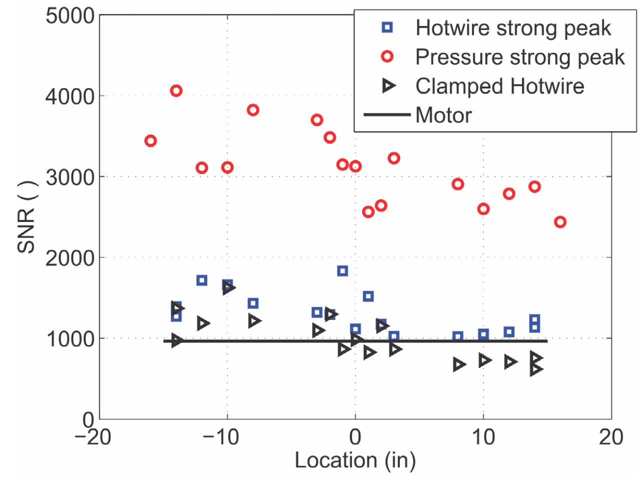

Figure 10. Spectral peak magnitude of the vertex-upwind aeroelastic response fo rteh 12-sided model,, Re = 44,000 ± 2000.

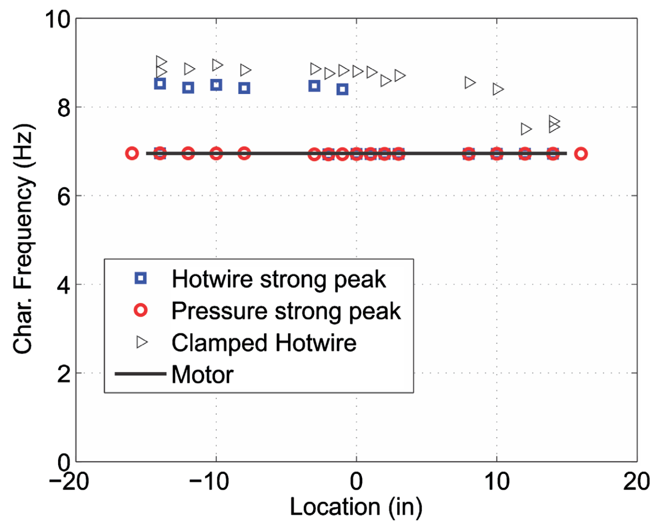

Figure 11. Face-upwind 12-sided model exhibiting lock-in at one location, Re = 44,000 ± 2000.

vortex cell were not overpowering the forced excitation or vice versa.

To further prove repeatability, a face-upwind study is shown in **Figure 11**. In this study, the qualitative results from the face upwind configuration are very similar to the vertex upwind case, however, in this case (since it is a face upwind configuration) the characteristic frequency of the vortex cell at the thin end of the model is 1 Hz lower in the stationary case and 1.5 Hz lower in the forced case. The data suggests the same trend: a vortex cell at the thin end of the model that drives the primary shedding frequency unless the shedding frequency is close enough to the forcing frequency to merge into the forcing frequency. In the previous case, there was a minimum of 1 Hz needed between the forcing and aerodynamic shedding frequency for most of the vortex cell to lock onto the forcing frequency. The face upwind case also shows a switch from the thinner end vortex cell aerodynamic shedding frequency to the forcing frequency at a thinner location on the tower. In the vertex upwind case, the change in frequency was intermittent near the boundary, but in the face upwind case, the switch appears more abrupt near the −5.08 cm span-wise location. Also, the characteristic frequency changes dramatically for the case of moving and stationary cases. This would explain the 0.5 Hz frequency disparity between the stationary and forced cases.

Figure 12 shows the signal strength at different locations of the model. This graph shows that none of the stationary (clamped) hot wire peaks are stronger than the forced hot wire peak. Also, the peak signal-to-noise ratio seems to increase the further into the "excited" vortex cell and tapers off a little near the maximum location (35.6 cm, thick end). There are two possibilities for this increase in signal-to-noise ratio phenomenon: the hot wire data from the forced case with the wind tunnel turned off was not getting picked right (which would have been seen in other similar cases) or the forcing and stationary aerodynamic frequencies are acting constructively to create a more powerful, more coherent vortex structure akin to the flutter phenomenon in wings. If that is the case, this is important for design purposes as it shows there is a peak location and distribution for the strength of the forced vortex cell. It is also of interest to point that the pressure seems to have a similar pattern in the opposite direction in the peak strength distribution.

4.2. Changing Forcing Frequency with Constant Shedding Frequency

This subsection discusses fixed aerodynamic shedding frequency while varying the forcing frequency on the model. For this case, the sensors used were two hot wires and the pressure scanner. Figure 13 includes the frequencies measured at all sensors along the span. The title of each graph explains the motor setting in terms of the analog motor controller. At the slowest excitation, 2.2 Hz, the aerodynamic and forcing frequency are uncoupled and the hot wire signals and most

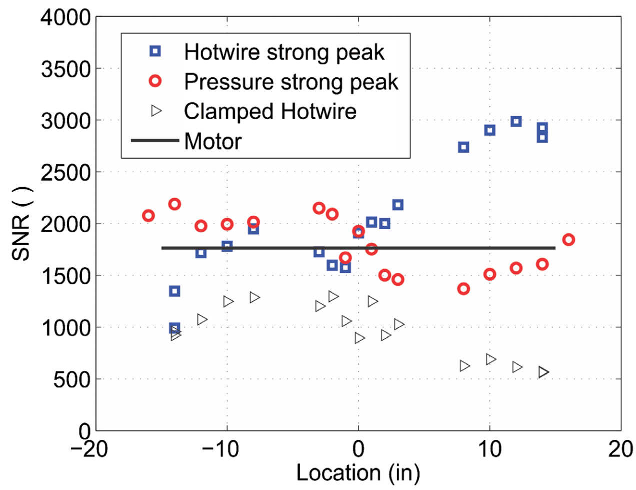

Figure 12. Peak strength with face upwind aeroelastic response for the 12-sided model, Re = 44,000 ± 2000.

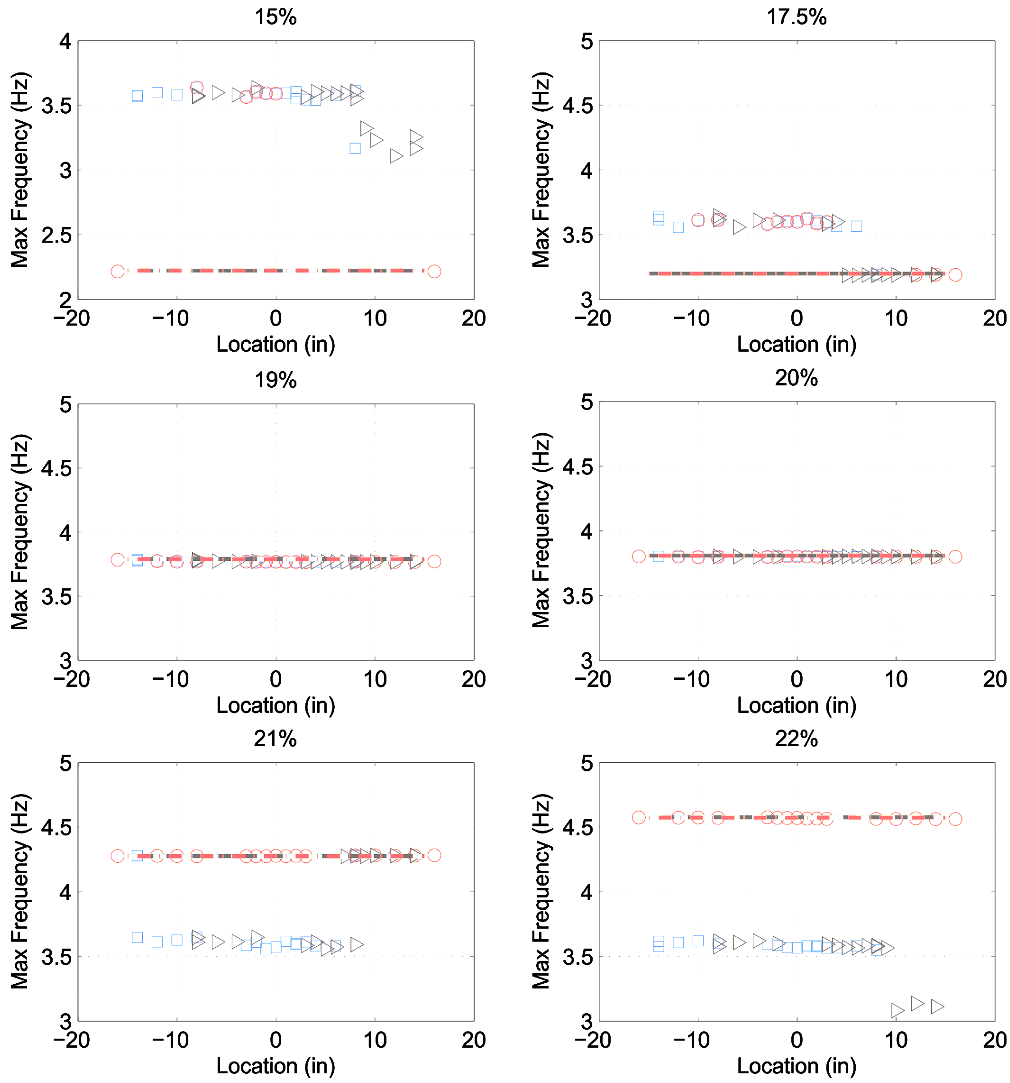

Figure 13. Forcing frequency comparison, Re = 16,300 ± 150, 12 sided model. Square is hot wire 1, triangle is hot wire 2, and circle are the pressure measurements, the line represents the motor frequency as confirmed by three sensors.

of the dominant frequencies in the pressure signals align with the stationary aerodynamic vortex shedding case. As the forcing frequency is increased to 3.2 Hz and reaches the shedding frequency of the thick end of the model, the thick end vortex cell locks in and the size of the thick end vortex cell increases by 13 cm, the boundary region increases from 5.1 cm 17.8 cm in this case. Increasing the forcing frequency even further (3.8 Hz) shows that now all the sensors are locked in with the thin end shedding frequency, that is, the size of the vortex cell has taken hold of the entire measurable model. The motor setting was then increased from 19% to 20% and the model was still completely locked in. When the forcing frequency is set 4.3 Hz, the thick end vortex cell continues to be locked into the forcing frequency but the frequency of the vortex cell near the thin end decouples and goes back to the frequency found in the stationary case. Finally, at 4.6 Hz, the flow reverts back to the original aerodynamic shedding for the hot wire sensors, but on the surface of the model the pressure fluctuations from the movement caused by the motor overpower the signal of the aerodynamic shedding from the movement of the shear layer.

Finally, when these graphs are organized in terms of percentage of lock-in and percentage of forcing frequency, the results show a graph that can be fitted to a cubic spline as seen in **Figure 14**. Consider too the case where 50% of the structure is locked in, then a range of forcing frequencies that are close to the aerodynamic shedding frequency can be derived. This range is between 10% to 15% of the aerodynamic shedding frequency. This measured range is significant because the different building codes use different ranges without such direct measurement. If this range is translated to a range of diameters and consequently a spanwise distance (using the taper ratio of 0.00117 cm/cm), the spanwise lock in is 299 cm. Thus, a structure that is 3000 cm tall will have a 10% spanwise lock in distance for a small perturbation of 0.254 cm.

5. Conclusions

The present paper describes a condition known as "lock-in" on a tapered structure with three different cross-sections. This document describes a phenomenon seen on high mast lighting towers where winds create oscillating tower-surface pressure fields at a single frequency regardless of local diameter. These pressure fields generate harmonic forces that resonate with the natural frequency of the structure, sometimes to catastrophic results. The phenomenon extracts energy from the airflow and transforms it into strain and kinetic energy in the tower, thus, as long as the air is flowing, the process is self-sustaining and grows as the

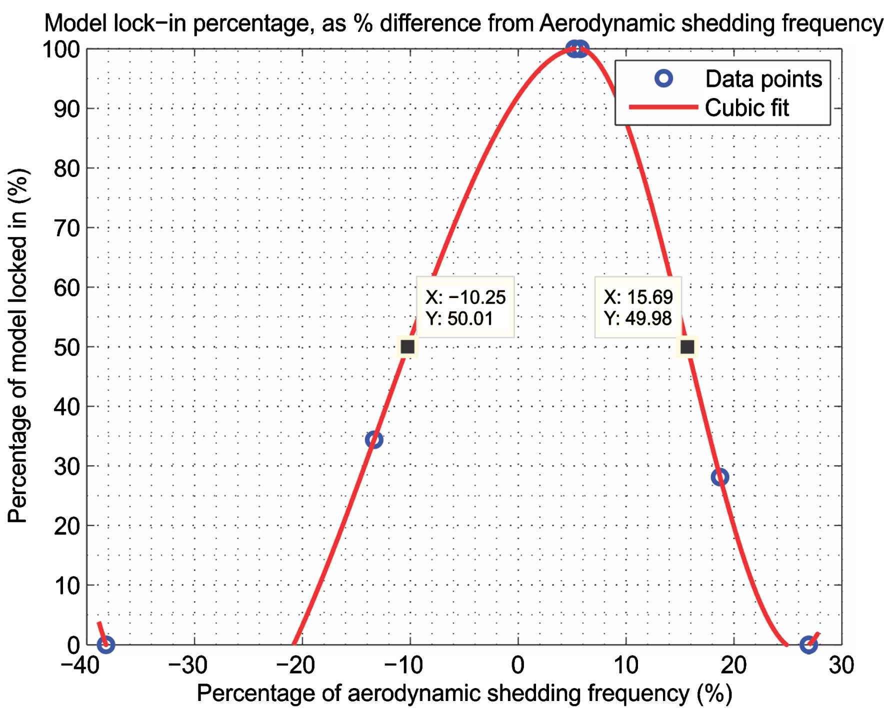

Figure 14. Amount of lock-in.

structure deflection increases with time, increasing the height-wise size of the vortex cells.

The wind tunnel research has reproduced the vortex cells phenomenon in the laboratory—same shedding frequency for different local diameters—and showed how much the addition of aeroelastic movement dictates the behavior and size of these vortex cells. The aeroelastic behavior depends on the proximity of shedding frequency to the forcing frequency.

Some of the conclusions reached in this study are that the vortex cell size (in the spanwise direction) has a dependence on frequency difference between forcing and stationary shedding frequency and that the forcing frequency (in this case the elastic movement frequency) has to be within 15% of the aerodynamic shedding frequency to lock in. This means a structure spanwise lock in of 305 cm for a typical HMLT.

Acknowledgements

The authors gratefully acknowledge support for this research from the NCHRP, project number 10-74.

Conflicts of Interest

The authors declare no conflicts of interest regarding the publication of this paper.

References

[1] Roshko, A. (1961) Experiments on the Flow Past a Circular Cylinder at Very High Reynolds Numbers. *Journal of Fluid Mechanics*, **10**, 345-356. https://doi.org/10.1017/S0022112061000950

[2] Every, M.J., King, R. and Weaver, D.S. (1982) Vortex-Excited Vibrations of Cylinders and Cables and Their Suppression. *Ocean Engineering*, **9**, 135-157. https://doi.org/10.1016/0029-8018(82)90010-5

[3] Repetto, M.P. and Solari, G. (2002) Dynamic Crosswind Fatigue of Slender Vertical Structures. *Wind and Structures*, **5**, 527-542. https://doi.org/10.12989/was.2002.5.6.527

[4] Ruscheweyh, H. (1994) Vortex Excited Vibrations. In: Sockel, H., Ed., *Wind-Excited Vibrations of Structures. International Centre for Mechanical Sciences*, Springer, Vienna, 51-84. https://doi.org/10.1007/978-3-7091-2708-7_2

[5] Connor, R.J., Collicott, S.H., DeSchepper, A.M., Sherman, R.J. and Ocampo, J.A. (2012) Fatigue Loading and Design Methodology for High-Mast Lighting Towers. The National Academies Press, Washington. https://doi.org/10.17226/22792

[6] Ericsson, L.E. (1985) Effect of Cross-Sectional Shape on the Response to Karman Vortex Shedding. *AIAA* 23*rd Aerospace Sciences Meeting*, Reno, 14-17 January 1985, 1-11. https://doi.org/10.2514/6.1985-448

[7] Higuchi, H., Anderson, R.W. and Zhang, J. (1996) Three-Dimensional Wake Formations behind a Family of Regular Polygonal Plates, *AIAA Journal*, **34**, 1138-1145. https://doi.org/10.2514/3.13204

[8] Phares, B., Sarkar, P., Wipf, T. and Chang, B. (2007) Development of Fatigue Pro-

cedures for Slender, Tapered Support Structures for Highway Signs, Luminaries, and Traffic Signals Subjected to Wind-Induced Excitation from Vortex-Shedding and Buffeting. Midwest Transportation Consortium.

[9] Noack, B.R., Ohle, F. and Eckelmann, H. (1991) On Cell Formation in Vortex Streets. *Journal of Fluid Mechanics*, **227**, 293-308. https://doi.org/10.1017/S0022112091000125

[10] James, W.D. (1983) Effects of Reynolds Number and Corner Radius on Two-Dimensional Flow around Hexdecagonal Cylinders. *AIAA 16th Fluid and Plasma Dynamics Conference*, Danvers, 12-14 July 1983, 1-11. https://doi.org/10.2514/6.1983-1705

[11] Bosch, H.R. and Guterres, R.M. (2001) Wind Tunnel Experimental Investigation on Tapered Cylinders for Highway Support Structures. *Journal of Wind Engineering and Industrial Aerodynamics*, **89**, 1311-1323. https://doi.org/10.1016/S0167-6105(01)00144-1

[12] Giosan, I. and Eng, P. (2007) Vortex Shedding Induced Loads on Free Standing Structures, Structural Vortex Shedding Response Estimation Methodology and Finite Element Estimation. https://citeseerx.ist.psu.edu/viewdoc/summary?doi=10.1.1.582.3179

[13] Vickery, B.J. and Clark, A.W. (1972) Lift or Crosswind Response of a Tapered Stack. *Journal of Structural Division*, **98**, 1-20. https://doi.org/10.1061/JSDEAG.0003103

[14] Gaster, M. (1969) Vortex Shedding from Slender Cones at Low Reynolds Numbers. *Journal Fluid Mechanics*, **38**, 565-576. https://doi.org/10.1017/S0022112069000346

[15] (2022) Valmont High Mast Lighting Poles. https://www.valmontstructures.com/products-solutions/lighting/high-mast-lighting-poles

[16] Ocampo, J.A. (2013) Vortex Shedding Lock-in on Tapered Bodies of Various Polygonal Cross-Sections. PhD Thesis, School of Aeronautics and Astronautics, Purdue University, West Lafayette.

[17] Kamen, E.W. (2000) Fundamentals of Signals and Systems. Prentice Hall, Upper Saddle River, New Jersey.

Appendices

A. Data Processing and Validation of Results

This section details the data processing for this paper. This includes a detailed breakdown of the different types of processing done to each raw voltage signal. There are four Matlab source code files that do the processing: three are functions and the fourth is the main file that calls on the functions and plots the data. This section will not delve into the line by line description of the code but will explain the overall process and show how the data processing gives clearer results. The functions and programs do have commenting on them, so reading through them will be easier.

A1. Overview of Data Process Method

The data processing was all done in Matlab after the data was taken. That way, the unfiltered, unprocessed data could be kept if needed at any point during the work or be processed differently later. When the data is collected from either the hot wires or pressure scanner through the oscilloscope, the points come out as a vector of voltages. The divisions per second and points per second are displayed in the header of the voltage file but there is no time vector in the output. Hence, a script was introduced in the reader Matlab source code file to extract the time divisions and automatically create a time vector output.

It would be useful to do a breakdown of the mathematical functions used through the different scripts to have an understanding of the overall changes done to the signal. The first part of the script reads the data and creates a voltage vector for each sensor used. Consequently, the vector (in Volts, referred to as V from now on) is an input for a windowing function. First, the mean must be removed, so Equation (1).

$$V_{new} = V - \frac{\sum_{i=1}^{N} V_i}{N} \tag{1}$$

where N is the total number of points in the vector. Then, the signal is windowed using a cosine window, w.

$$w = 0.5 * \frac{1-\cos\left(2\pi\left[0:(N-1)\right]\right)}{N-1} \tag{2}$$

After the function is windowed, the vector is padded with zeros,

$$V\left((N+1):(8N)\right) = 0 \tag{3}$$

The filter used is a second order low-pass Butterworth filter, the frequency response is given by

$$H_{jw} = \frac{1}{\sqrt{1+\left(w/w_n\right)^2}} \tag{4}$$

where w_n is the cutoff frequency and $w = 2\pi f$ [17]. Next, the primary peak location and magnitude is found using the built in Matlab function max. The function then goes through a process of finding the power spectra by using a Fast Fourier Transform in Matlab and finding the maximum location.

$$V_{FFT} = \sum_{n=0}^{N-1} V(n)\exp(-j2\pi kn/N) \quad (5)$$

where V is the original signal, k = 0, 1, ..., N 1, n is the dummy variable for summation, N is the total size of the vector [17]. Then, the area around the peak is equated to 0 to find the next peak.

$$V\left(\left(f_{peak} - 0.1\right):\left(f_{peak} + 0.1\right)\right) = 0 \quad (6)$$

and the max function is used again to get the next strongest peak. Sometimes, when there is a single strong peak, the function will return a value 0.1 Hz from the primary peak, meaning there are no more peaks in the spectra. The noise and signal-to-noise ratio are calculated.

$$Noise = mean(V)\,SNR = max(V)/Noise \quad (7)$$

These values are then set as outputs and can be plotted. The process is repeated for every pressure and hot wire signal to compile a full spanwise scan.

Figure 15 shows a graphical representation of the process shown in the mathematical section.

In the first part, the program calls on the mproc.m file which is a function to process each individual signal. Within mproc.m, the signal is read using custom function lcread.m, this function reads the original oscilloscope file and creates a time vector and nx4 matrix, where n is the number of data points and 4 represents the 4 channels of the oscilloscope. The data then goes back to mproc.m where it is divided into 1 to 4 voltage vectors (for each of the channels being used) and passed through winzeropad.m to subtract the mean, window, and zero pad the signal before filtering. The variables returned to mproc.m are a new frequency vector (for the new zero padded signal) and the new voltage vectors. The FFT of the new voltage vectors is then taken, and subsequently filtered using a low-pass Butterworth filter. Finally, function findpeak.m is used to find the peak of the signal and use quadratic interpolation to find the sub-bin frequency location of the peak. This is only done when the signal to noise ratio of the peak is above 3. If it is less, the program returns a "too much noise" message and a value of zero for the frequency at the peak. The function checks for the location of the largest peak so sometimes (when electrical interference may be large) it will show a frequency of 60 Hz for the peak frequency. In these cases, the researcher has manually checked locations and reduced the low-pass frequency filter to obtain the correct frequency. After finding the first peak, the frequency range within 0.1 Hz is equated to zero and the next highest peak is found. Then, the noise is calculated as the mean of the entire signal and the signal-to-noise ratio (SNR) at each of the two peaks is found. These are set as outputs for the findpeak.m function and sent to mproc.m which compiles all the spectra, peak locations, and SNR, and outputs to the main program. The program then plots the results.

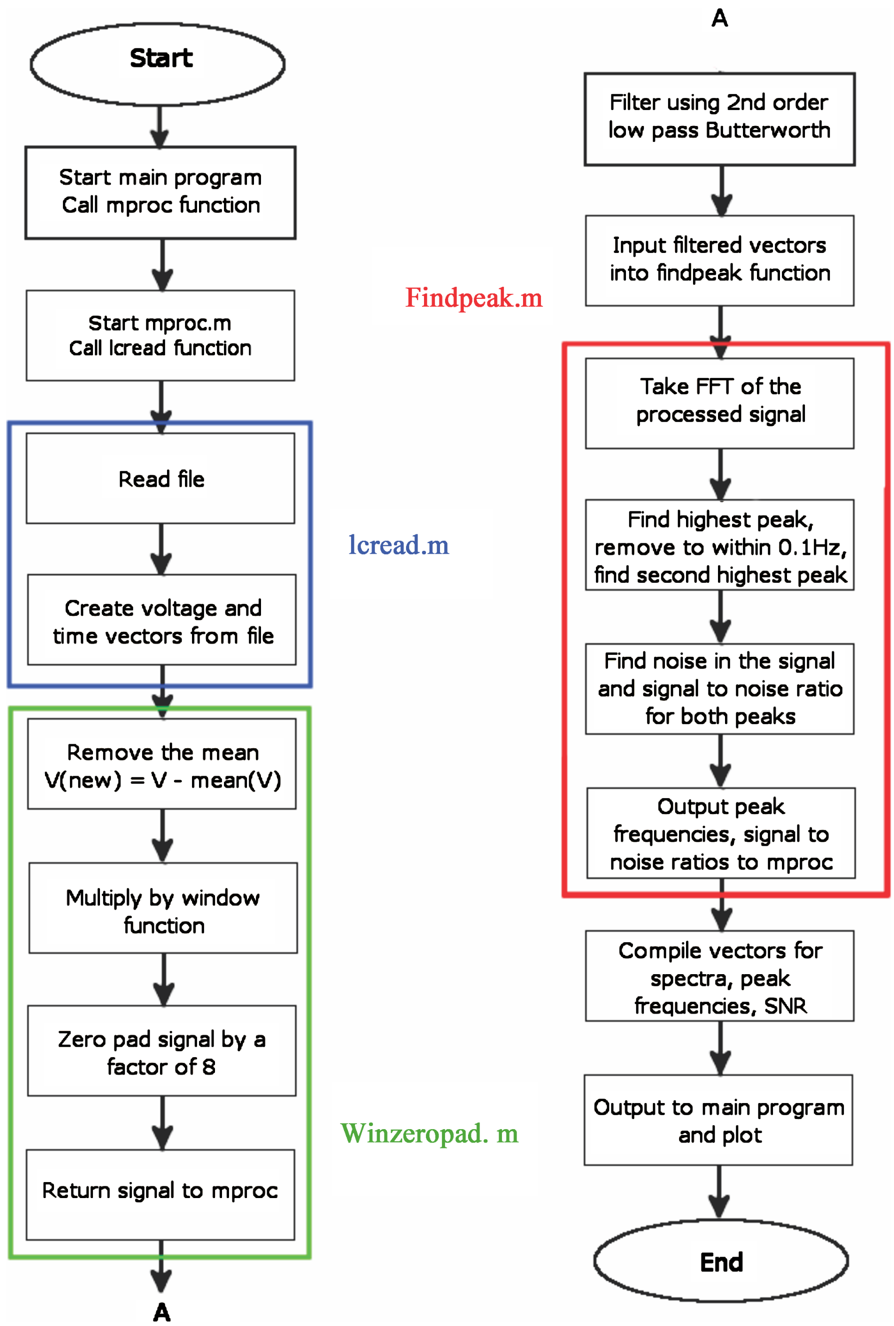

Figure 15. Flowchart of the signal processing method.

A2. Subtracting the Mean and Windowing

The first two parts of the processing include subtracting the mean and using a window function. There are several functions that can be used including Cosine, Blackman, 4-term Blackman-Harris, Hann, Bartlet-Hann, Hamming, and Keiser-Besel. The winzeropad.m m-file function includes the option to use any of these windowing functions, and a study of a typical voltage signal FFT with these different filters can be seen in Figure 16.

As is seen in Figure 16, the location of the peak and shape of the FFT does not change with window option except for the Keiser-Besel case. Thus, a cosine window was used to process the data. One reason to subtract the mean before windowing is to avoid the creation of a "cosine" arc that creates a large spike at 1 Hz. This is easier to visualize with a picture so Figure 17 is included.

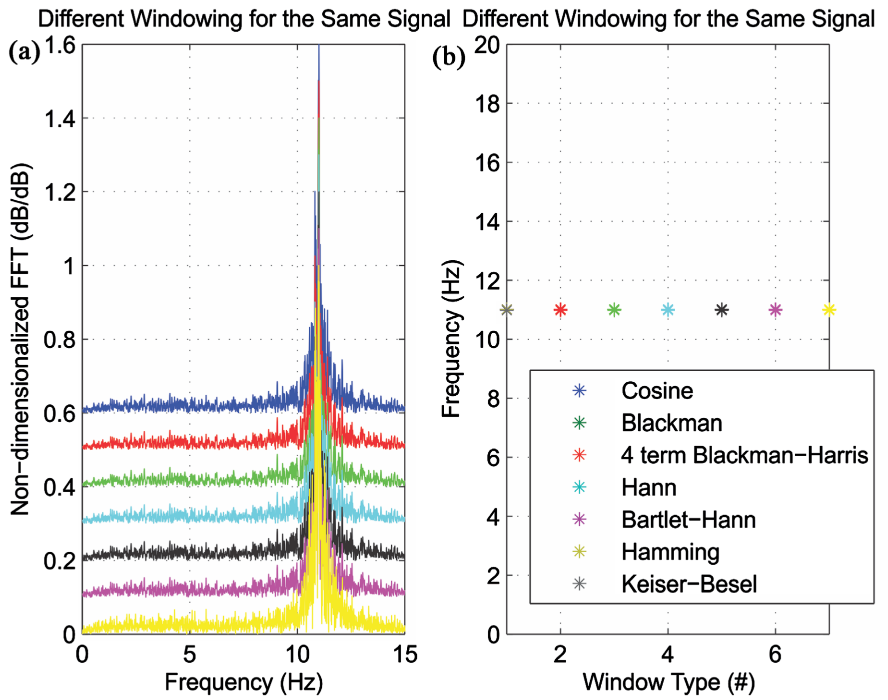

Figure 16. (a) The different spectra for different windows. b) The peak location processed for the same signal with different window functions.

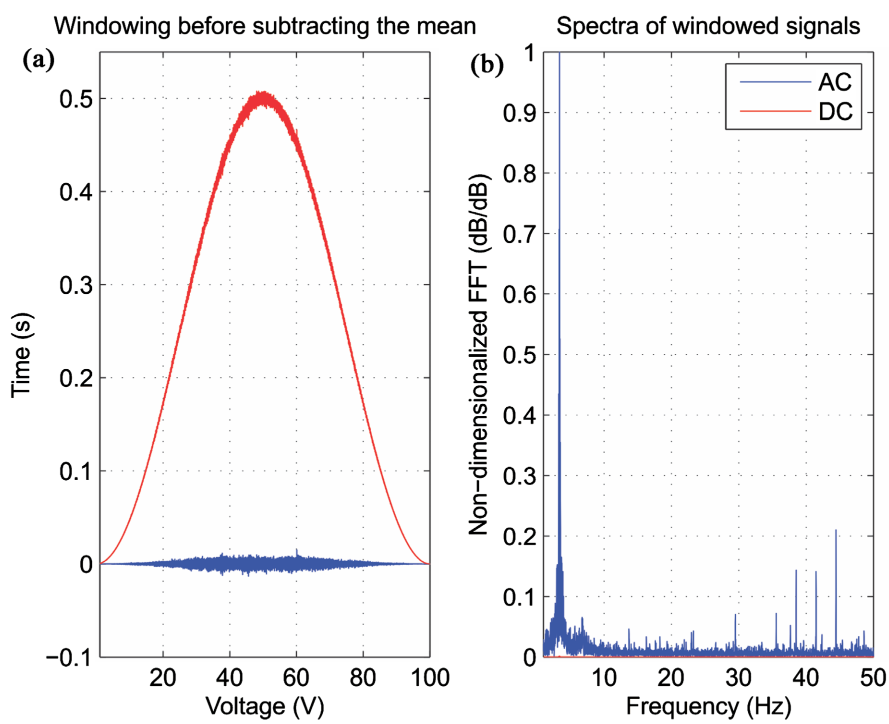

Figure 17. (a) Windowed DC signal with and without mean removed. (b) Spectrum of the signal with and without mean removed.

When the mean is not removed, the FFT plot has a spike that overshadows all the relevant frequencies. The FFT for the signal windowed without removing the mean just looks like there is no peak and there are no relevant frequencies. When the mean is subtracted however, the peak created near 0 is removed and this allows the relevant frequencies to show. If windowing is done before subtracting the mean, the signal will become a large arc that grows near the middle. However, as the mean is removed, the signal becomes 0 at the beginning and end and grows near the middle. The windowing function used is shown in Equation (4).

A3. Zero Padding

The next step is zero padding. Zero padding is the addition of a vector of zeros to the end of the signal, essentially creating a larger vector for the FFT than before. It is important to note that this step is done after windowing and subtracting the mean. This ensures that the end of the windowed signal can transition nicely into the zero padded vector. Adding this sets of zeros increases the computing cost of the FFT but adds "intermediate" points in the FFT horizontal axis that make the peak clearer and enhance the accuracy of the quadratic interpolation done later. For example, in the original signal, there may be a point at 20 Hz and another at 20.1 Hz, but with zero padding, there will be a point at 20, 20.02, 20.04, 20.06, 20.08, and 20.1 Hz in essence increasing resolution on the horizontal axis. An example of a zero padded signal can be seen in **Figure 18**. In the non-padded signal, the location of the peak is at a jagged peak, while with zero

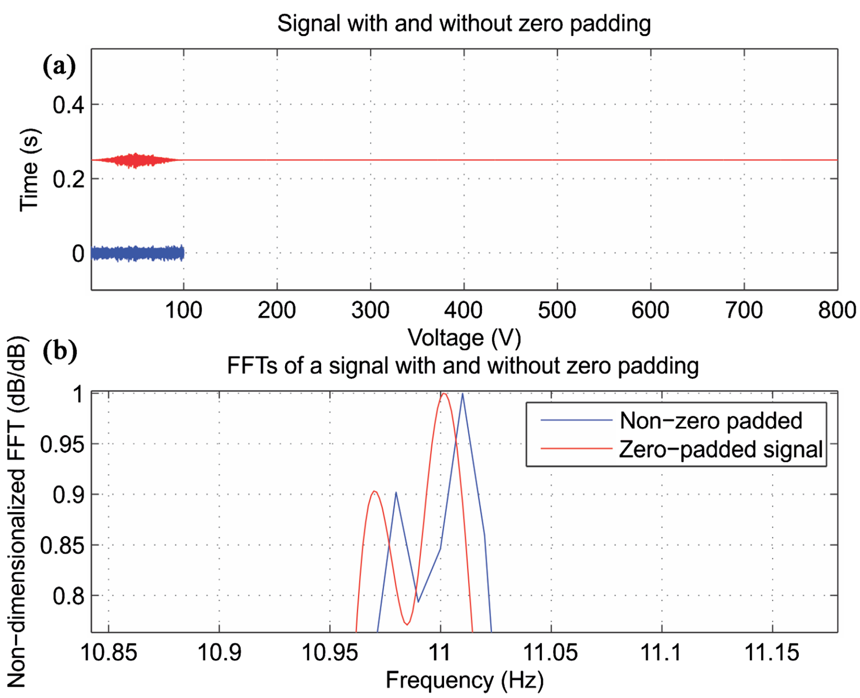

Figure 18. (a) Zero padded signal comparison to non-padded signal. (b) Zero padded FFT peak zoom comparison to non-padded signal, the FFT is slightly offset to better appreciate the changes.

padding, the same signal shows a bell-shape frequency peak making finding a peak more accurate.

A4. Filtering

The mproc.m file includes a low-pass Butterworth filter (the default filter in Matlab). This low-pass filter is used to remove signals at higher frequencies than the characteristic frequency or its lower order harmonics. Thus, the sources of aerodynamic or ambient noise are removed. The Butterworth filter includes two variables: the first being the order of the Matlab filter (in this case, 2), and the second variable describes the cutoff point for the low-pass filter. Other orders of filters were tried but were slower and did not deliver significant improvements. One such example is shown in **Figure 19**.

In here the reader can see a small difference between the two cutoff frequencies due to the order of the filter but not on the location or signal to noise ratio of the characteristic peak. The filters were applied so the results could be seen in **Figure 19** (at a frequency of approximately 40 Hz) but are usually set to taper off at higher frequencies so important frequencies such as the first and second harmonics are not lost in the filtering process.

Bear in mind most of these signals are 1000 samples per second meaning a 20% low-pass filter only cuts out noise that is far from the characteristic frequency or its first harmonic. Characteristic frequency is in the 2 - 20 Hz range, and the filter reduces the signal from 50 Hz to 500 Hz. This reduces noise seen in separated areas of air, where recirculation is commonly seen for the pressure scanner signals.

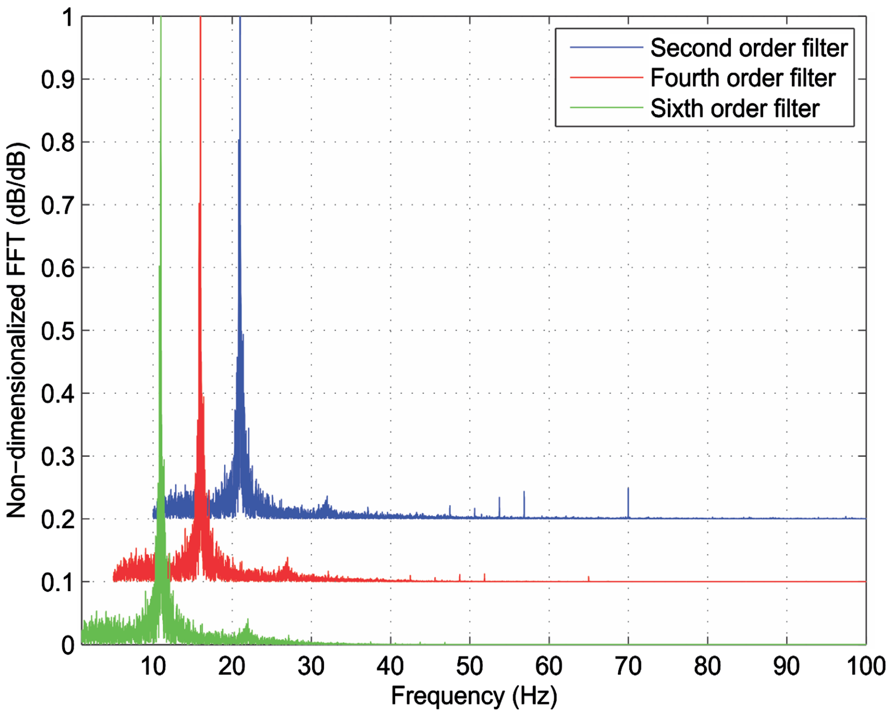

Figure 19. Impact of different order filtes on the final results.

A5. Quadratically Interpolated FFT (QIFFT)

Finally, the Quadratically Interpolated FFT (QIFFT) is used in the function findpeak.m. Using curve fitting of four points, we can get sub-bin accuracy on the location of the peak by modeling the four points as a continuous curve. This however only works if there is enough horizontal resolution to start with. The quadratic interpolation uses the three points that are closest to the peak plus a fourth point that is either higher or lower frequency depending on the vertical location of the peak. Figure 20 shows how the program chooses which 4th point to use.

From there, equation (9) used to do the fitting is "polyfit" from Matlab which uses a least squared method to find the best fit of a set of two vectors.

$$polyfit\left(X,Y,N\right) \tag{9}$$

where X is a vector of points, Y is the corresponding y-value for the points in X, and N is the order of the equation (1 for linear, 2 for quadratic, etc..). After the polyfit equation coefficients are found, the program creates a vector of fine points with the coefficients and finds the maximum. The results are usually within 2% of the previous maximum peak found after zero-padding. This method is used to further reduce error.

B. Comparison of Processed and Unprocessed Results

The final comparison of the processed and unprocessed results can be seen in Figure 21. The final result gives a more accurate FFT peak location and cleans up the multiple peaks seen in the original unprocessed signal. This makes it easier to define the true peak and reduces false peaks created by noise on the signal during the FFT processing. The method also allows for clearer frequency peaks at different locations, such as at the interaction between two vortex cells and reduces the noise between the two characteristic peaks.

B1. Stability of the Signal

This section deals with how stable the aerodynamic shedding of the signal is in the spanwise center of the vortex cell. To do this, a 500 second signal is broken down into 500 1-second pieces and the spectra of each of these 500 data streams is computed. The wind tunnel velocity for this signal is unchanged throughout the test and the model is clamped throughout the test. Three different tests at different times on different days but with the same model were done. The results

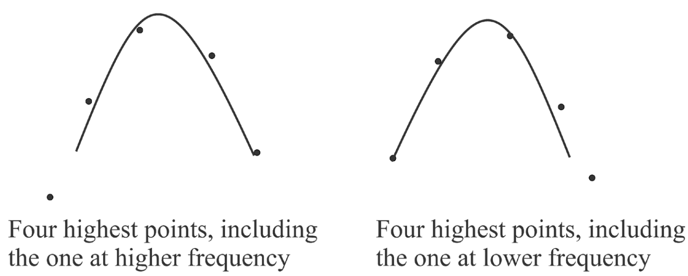

Figure 20. Illustration of how the quadratic interpolation algorithm chooses the 4th point.

for these tests can be seen in **Figure 22**.

Figure 22 shows the three signals close together and the change in signal frequency being, on the most part, less than 5% meaning a frequency of 11 Hz and a signal of 9 Hz would be too much of a gap for a continuous signal change unless aerodynamically they were fundamentally different.

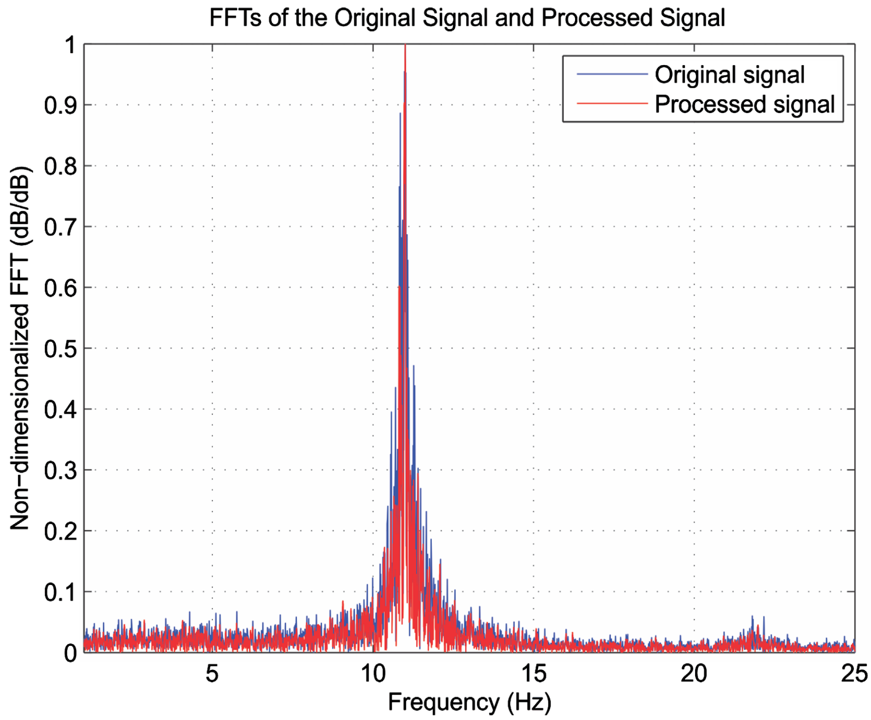

Figure 21. Processed versus unprocessed signal and spectra.

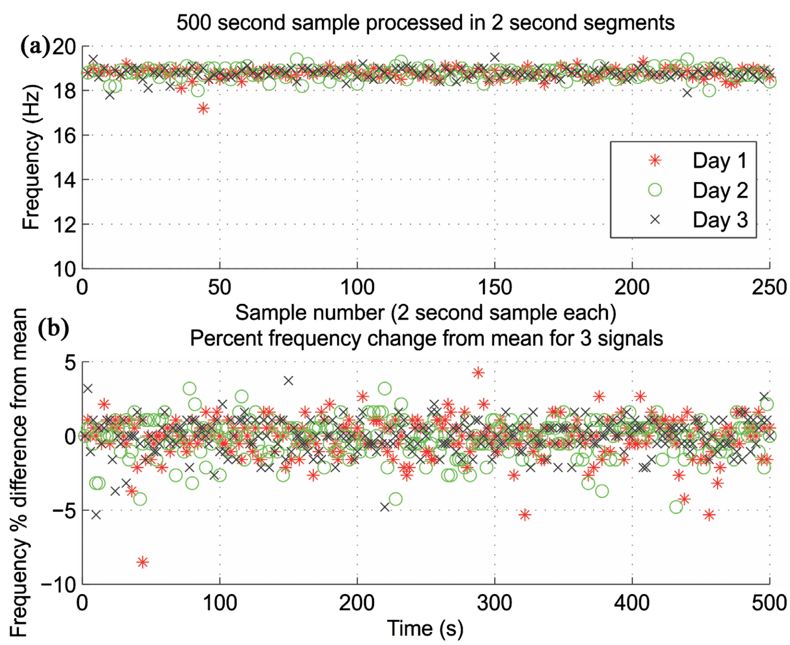

Figure 22. (a) Frequency taken on different days after dismounting and re-mounting model. (b) Error % difference between the frequency found and mean.

B2. Validation Using Circular Cylinder Data

One way to validate the data processing is using well known circular cylinder data from literature and comparing it to experimentally acquired data for a circular cylinder in the Boeing wind tunnel. The data was taken at different velocities and broken into 1 second signals. To do this, the tunnel was turned on at the maximum velocity for a long duration test (around 18 m/s or 35 Hz on the motor setting) and was slowly manually reduced in speed while taking a 500 second duration signal at 1000 samples per second. This way, the change in frequency was gradual and the 1 second signals have approximately constant frequency. Another way of doing this was turning the tunnel off and letting the air go down to rest on its own but this has drawbacks. If the tunnel was turned off, the frequency change would have been faster and there could be overlap of two (or a range of) frequencies (one during the first 500 ms and another on the other 500 ms of the one second signal block), this could not be resolved with the find peak function and was thus deemed less suitable than the slow deceleration approach. Figure 23 shows the velocity versus frequency plot.

The frequency at each velocity was taken and a Reynolds vs. Strouhal plot was compiled. In theory, the area between 103 < Re < 105 has a small downward slope. The results seen in the cylinder data are thus in accordance with established theory. An estimation of these upper and lower bounds is included in Figure 24 for clarification. Another datum of interest is that the percent error from the QIFFT increases with increasing velocity. This means that results at lower velocities are not as accurate as those at higher speeds and thus higher

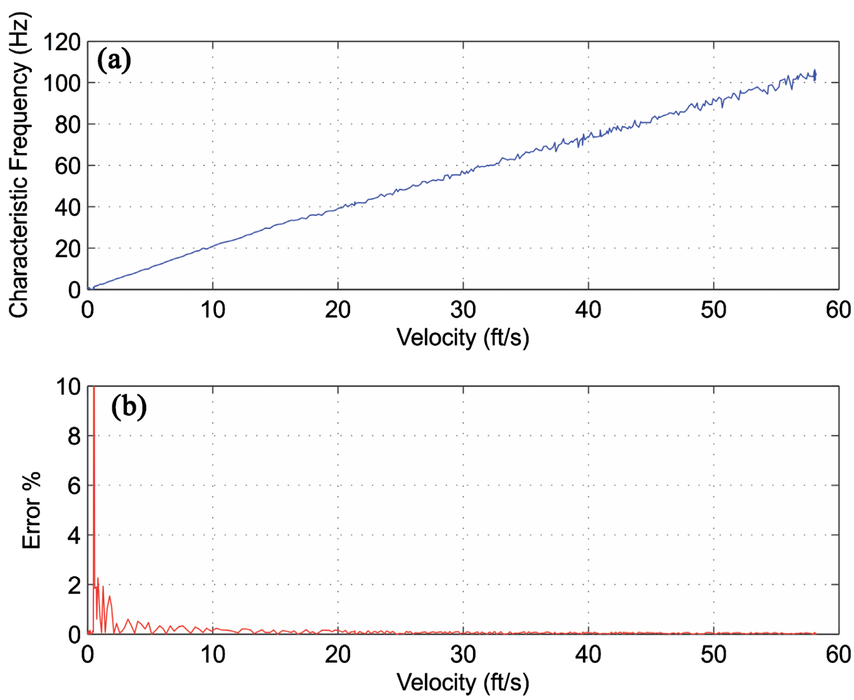

Figure 23. (a) Velocity versus shedding frequency for a circular cylinder, linear fitting done near zero (V < 1.5 ft/s) due to picking up noise over shedding frequency signal. (b) Error % difference from QIFFT.

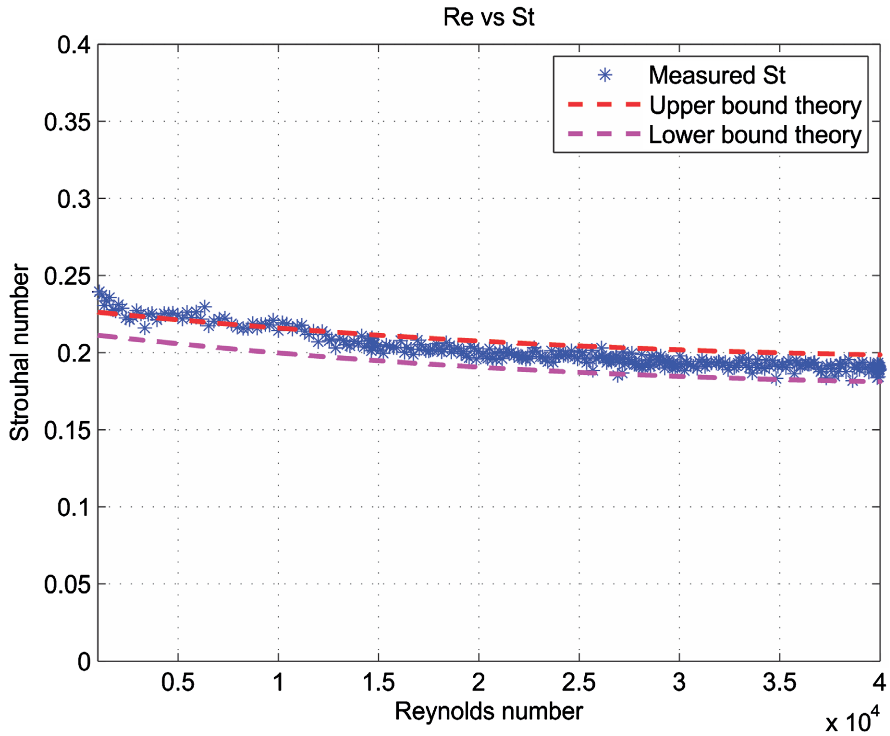

Figure 24. Measured Strouhal number versus Reynolds number for a circular cylinder compared to theoretical values

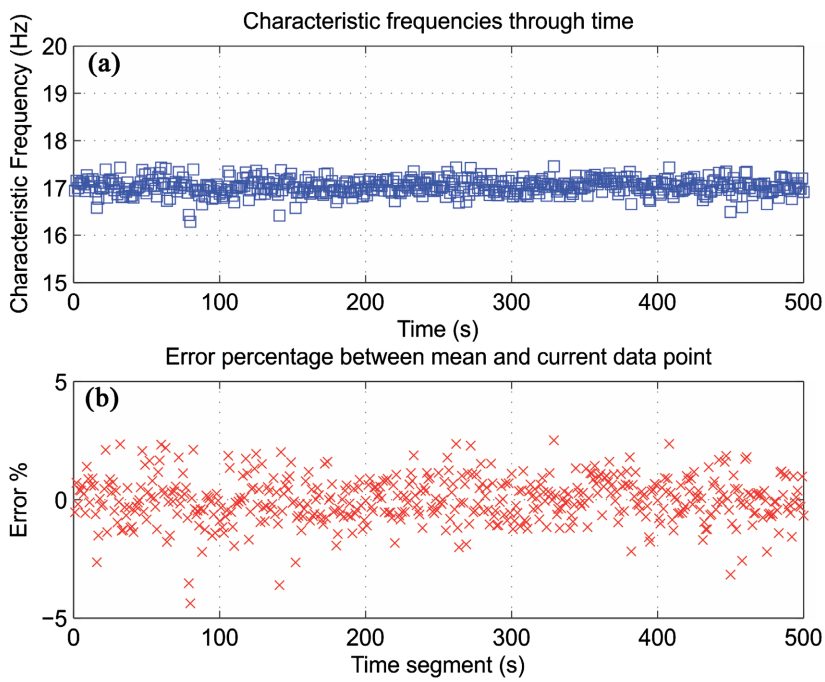

Figure 25. (a) Frequency peak location for 500 seconds on circular cylinder. (b) Percent error between current frequency and mean over 500 seconds.

frequencies. However, looking at the frequency versus speed plot, we can see that there is more frequency variation near the high end of the spectrum than near the low end.

Note too that the stability of the vortex shedding study was done on the circular cylinder. A constant wind tunnel velocity, clamped-configuration test was done with the circular cylinder for 500 seconds. The signal was then broken down into 500 one-second segments and individual FFTs for each segment were computed. The result of those studies can be seen in **Figure 25**.

Figure 25 shows how the signal changes with time and the average change in percentage to the mean. The changes with respect to the mean are very small (on the order of 0.1%) so the signal is relatively stable. It also shows that even though there is a change in the tunnel air temperature (the tunnel heats up with time) there is no noticeable change on the shedding frequency. The error is thus approximately 2-3% from the mean, and significantly smaller when looking at a full 100 or 500 second signal since some of those error fluctuations are averaged out.